

See discussions, stats, and author profiles for this publication at: <https://www.researchgate.net/publication/231270660>

Yield Optimization and Scaling of Fluidized Beds for Tar Production from Biomass

ARTICLE *in* ENERGY & FUELS · JULY 2001

Impact Factor: 2.79 · DOI: 10.1021/ef010053h

CITATIONS

37

READS

5

2 AUTHORS, INCLUDING:



[D. Lathouwers](#)

Delft University of Technology

88 PUBLICATIONS 452 CITATIONS

SEE PROFILE

Yield Optimization and Scaling of Fluidized Beds for Tar Production from Biomass

D. Lathouwers[†] and J. Bellan^{*}

*Jet Propulsion Laboratory, California Institute of Technology,
Pasadena, California 91109-8099*

A numerical study is performed in order to evaluate the performance and optimal operating conditions of fluidized bed pyrolysis reactors used for condensable tar production from biomass. For this purpose, a previously validated biomass particle pyrolysis model is coupled with a detailed hydrodynamic model for the binary gas particle mixture. The kinetics scheme is based on superimposed cellulose, hemicellulose, and lignin reactions. Any biomass feedstock can be simulated through knowledge of its initial mass composition with respect to these three primary components. The separately validated hydrodynamic model is based on a three-fluid model (gas, sand, and biomass) derived from the kinetic theory of granular flows. Separate transport equations are constructed for each particle class, allowing for the description of such phenomena as particle segregation and for separate temperatures for each particle class. The model is employed to investigate the effect of various operating conditions on the efficiency of tar collection in fluidized bed reactors. Results indicate that, at fixed particle size, the operating temperature is the foremost parameter influencing tar yield. The biomass feed temperature, the feedstock, and fluidization velocity magnitude, all have minor impact on the yield. The particle diameter has a considerable influence on the short-time tar yield, but it is inferred that it may have a more moderate influence on the steady-state tar yield. For the range of fluidizing gas temperatures investigated, optimum steady-state tar collection is obtained for 750 K under the assumption that the pyrolysis rate is faster than the feed rate; the predicted optimum temperature is only slightly higher if this assumption is not satisfied. Finally, scale-up of the reactor is addressed and is found to have a small negative effect on tar collection at the optimal operating temperature. It is also found that slightly better scaling is obtained by using shallow fluidized beds with higher fluidization velocity.

1. Introduction

The interest in clean hydrogen fuel production has triggered substantial activity in high temperature biomass pyrolysis in many countries. The aim of these activities is to obtain a process that maximizes tar yield while simultaneously minimizing char formation. Biomass pyrolysis involves the heating of raw biomass in the absence of an oxidizer in order to extract reaction products for subsequent processing. Among several reactor geometries, the vortex reactor and the fluidized bed reactor were the subject of research activities at the National Renewable Energy Laboratory (NREL), being potentially attractive as commercial pyrolysis devices. The vortex reactor was the subject of an earlier study (Miller and Bellan¹) accomplished by coupling a detailed model for pyrolysis to a fundamental fluid dynamics model of the vortex reactor. A similarly fundamental and detailed study of the pyrolysis conditions in a bubbling fluidized bed is not available in the literature.

The fluidized bed reactor consists of a cylindrical

vessel partially filled with sand. The sand's main purpose is to provide a large heat reservoir to keep the mean temperature of the bed constant. In turn, heat has to be provided to the biomass, as the pyrolysis is an endothermic process. This is achieved by heating the walls of the reactor and by injecting hot steam or nitrogen which is further used to fluidize the mixture, while also preheating it. The fluidizing gas induces a violent gas and solid flow pattern in the reactor, with both locally dense and void particle regions. An overall circulative complex flow occurs, explaining the excellent mixing behavior of fluidized bed reactors. Fresh, relatively cool biomass is injected into the reactor through a feeding mechanism in the wall, or directly into the bed using an injection "rod". After the biomass is fed into the reactor, it partially mixes with the sand and heats. As heating progresses, the particles pyrolyze and eject product gases (tar and gas; gas denotes here the collection of gaseous products complementary to tar) while at the same time forming char, which maintains the particle matrix. Product gases mix up with the fluidizing gas and are transported toward the reactor exit after which they are cooled to prevent product degradation, making collection of the condensable tars possible. To prevent degradation of product tars within the reactor, it is important to achieve small residence

^{*} Author to whom correspondence should be addressed. E-mail: josette.bellan@jpl.nasa.gov.

[†] Current address: Interfaculty Reactor Institute, Delft University of Technology, Mekelweg 15, 2629 JB Delft, The Netherlands.

(1) Miller, R. S.; Bellan, J. Numerical simulation of vortex pyrolysis reactors for condensable tar production from biomass. *Energy Fuels* **1998**, *12* (1), 25–40.

times for the gaseous pyrolysis products. Finally, remaining particles containing char erode to smaller size grains and are carried out of the reactor by the gas flow. This self-cleaning feature makes fluidized bed reactors especially suited to continuous operation.

Despite the attractive simplicity of the reactor design, no thorough analyses are available of fluidized pyrolysis reactors addressing issues such as efficiency, optimal operating conditions, and scale-up for commercial use. Although the literature addressing the modeling of the biomass fluidized bed reactor is virtually absent, experimental studies (Scott and Piskorz^{2,3}) have shown its potential for condensable tar production. These studies, however, have primarily focused on bench and pilot scale setups, not focusing on commercial size operation.

In this paper, we present quantitative results from numerical simulations of both pilot scale and commercial scale fluidized bed reactors under viable operating conditions. These simulations are obtained from the coupling of a realistic biomass kinetics model with a detailed hydrodynamic model for the gas/particle mixture. Of particular interest are a quantitative assessment of parametric effects, optimal conditions, and scaling potential. The individual submodels, i.e., kinetics and hydrodynamics, have been appropriately validated against experimental data in previous publications (Miller and Bellan,⁴ Lathouwers and Bellan⁵). Favorable comparisons for these submodels lends support to confidence and validity of the overall model.

The paper is organized as follows: A summarized description of the kinetics and hydrodynamic submodels is given in Section 2; more details are available elsewhere (Lathouwers and Bellan^{5,6}). Section 3 describes the specifics of the fluidized bed reactor under consideration and contains the reactor simulation results and parametric studies. The parameters studied are the fluidizing gas temperature, initial biomass particle temperature, feedstock, fluidization velocity magnitude, particle size, and reactor scaling. A summary and conclusions are provided in Section 4.

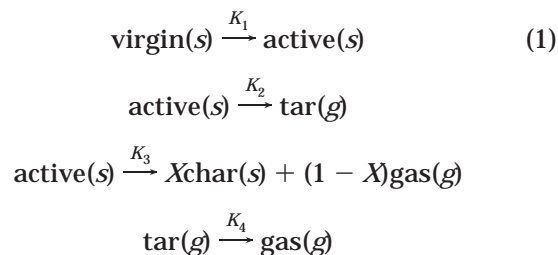
2. Model Formulation

As previously stated, the model developed by Lathouwers and Bellan⁶ consists of coupled submodels of the biomass kinetics and of the hydrodynamics of the gas particle mixture. The succinct description of these submodels is addressed below.

2.1. Single-Particle Biomass Pyrolysis Model.

The particle pyrolysis model employed here is that of the detailed kinetics derived by Miller and Bellan,⁴ based on superimposed cellulose, hemicellulose, and lignin reactions. This enables the simulation of different biomass feedstock through knowledge of the initial mass

composition with respect to these three primary components; biomass impurities are lumped with the hemicellulose as this model correlated best with the experimental data. Each of the virgin components undergoes the same generic competitive reaction scheme:



As indicated in the above kinetic scheme, the virgin components, the active intermediates, and the char are solid-phase species, while tar and gas are vapor products; these species are not pure chemical species but instead represent groups of compounds. All reactions are modeled with first-order Arrhenius kinetics; $K_i = A_i \exp(-E_i/RT)$, where the rate constants, A_i , activation energies, E_i for reactions K_1 , K_2 , K_3 , and the mass ratio X are dependent on the particular component, whereas all heats of reaction and secondary tar decomposition parameters (K_4) are independent of the source component.

This kinetic model combined with a porous particle flow dynamics model yielded validated predictions on tar/char yields ranging from the kinetically controlled regime (micro particles) to the diffusion controlled limit (macro particles), cf. Miller and Bellan.⁴ In the present paper, for simplicity, the biomass pyrolysis is assumed kinetically controlled. This assumption may be justified in the dense particulate regime where contact between particles may induce fragmentation (see Miller and Bellan¹ for a fragmentation model) and reduce the size of the particles to the point where the internal temperature equilibrates rapidly. Thus, the particle temperature, its mass and composition (global solid mass fractions) completely describe the state of the particle.

The sand and biomass particles are both solid and hence thermodynamically belong to the same phase. They, however, have different physical properties and different temperatures, etc. In particular, the biomass particles are porous whereas the sand particles are not. Therefore we solve separate equations for these particle classes.

2.2. Hydrodynamic Model. The hydrodynamic model describing the dynamics of the gas particle mixture is that derived by Lathouwers and Bellan.⁵ In previous papers (Lathouwers and Bellan^{5,6}), the model was applied to a variety of test cases in order to quantify its predictive capabilities. These included (i) comparison of the stresses generated by the shearing of a homogeneous particle mixture, (ii) comparison of the particle pressure generated along the wall of a bubbling fluidized bed, (iii) the characteristic behavior of monodisperse and binary homogeneously fluidized beds, and (iv) biomass particle pyrolysis in a fluidized bed reactor. Here, we give a brief description of the model, referring the reader for full details to the derivation of Lathouwers and Bellan.⁶

The hydrodynamic model is based on a three-fluid model description where macroscopic transport equa-

(2) Scott, D. S.; Piskorz, J. The flash pyrolysis of Aspen-polar wood. *Can. J. Chem. Eng.* **1982**, *60*, 666–674.

(3) Scott, D. S.; Piskorz, J. The continuous pyrolysis of biomass. *Can. J. Chem. Eng.* **1984**, *62*, 404–412.

(4) Miller, R. S.; Bellan, J. A generalized biomass pyrolysis model based on superimposed cellulose, hemicellulose and lignin kinetics. *Combust. Sci. Tech.* **1997**, *126*, 97–137.

(5) Lathouwers, D.; Bellan, J. Modeling and simulation of bubbling fluidized beds containing particle mixtures. *Proc. Combust. Inst.* **2000**, *28*, 2297–2304.

(6) Lathouwers, D.; Bellan, J. Modeling of dense gas-solid reactive mixtures applied to biomass pyrolysis in a fluidized bed. *Int. J. Multiphase Flow*, submitted.

tions are derived from the kinetic theory of granular flows using inelastic sphere models, thereby accounting for collisional transfer in high-density regions. Separate transport equations are constructed for each of the particle classes, allowing for the independent acceleration of the particles in each class and the interaction between size classes, as well as for the interaction processes whereby momentum and energy are exchanged between the respective classes and the carrier gas.

2.2.1. Definitions and Averaging. The continuum model was derived by Lathouwers and Bellan⁶ applying separate averaging procedures to both the carrier gas and solid phases. A phase ensemble average was used for the carrier phase, combined with a particle ensemble average where particle properties, such as velocity, are directly averaged. This procedure is attractive when resolution of the detailed degrees of freedom of the particles (e.g., internal temperature profiles or profiles of the internal chemical composition) is undesirable or unnecessary.

The general ensemble average of a field quantity $\Psi(\mathbf{x}, t)$, (\mathbf{x}, t denoting space and time coordinates) is

$$\langle \Psi(\mathbf{x}, t) \rangle = \int \Psi(\mathbf{x}, t) P(\Pi) d\Pi \quad (2)$$

where $P(\Pi)$ is the probability that a specific realization Π is encountered in the ensemble. The gas-phase ensemble average and its density-weighted counterpart are defined (Drew⁷) as $\bar{\Psi} \equiv \langle \chi_g \Psi(\mathbf{x}, t) \rangle / \alpha_g$ and $\bar{\Psi} \equiv \langle \chi_g \rho_g \Psi(\mathbf{x}, t) \rangle / \alpha_g \bar{\rho}_g$, where ρ_g is the gas density, χ_g denotes the phase indicator of the gas phase which is unity in the gas phase and zero otherwise, and the gas-phase fraction, α_g , is defined as the ensemble average of the indicator function, i.e., $\alpha_g = \langle \chi_g \rangle$. Average transport equations for the gas phase then follow by multiplying the local instantaneous equations (the Navier Stokes set supplemented with energy and species equations) by the phase indicator and ensemble averaging.

The transport equations for the solids were derived similarly to those for dense gases, using kinetic theory concepts. Important differences from classical kinetic theory are the inelasticity of collisions between macroscopic particles leading to dissipation, and the presence of an interstitial gas exerting drag on the particles, which leads to interaction terms in the averaged transport equations.

Let $f_i^{(1)}(\mathbf{x}, \mathbf{c}, Y_\xi, T, m, t)$ denote the single particle distribution function of particle class i such that $f_i^{(1)}$ is the probable number of particles of class i having their center of mass in the region $[\mathbf{x}, \mathbf{x} + d\mathbf{x}]$, a velocity in the region $[\mathbf{c}, \mathbf{c} + d\mathbf{c}]$, mass in the region $[m, m + dm]$, mass fractions in $[Y_\xi, Y_\xi + dY_\xi]$, and temperature in $[T, T + dT]$. With this distribution function, a particle average is introduced as an integration over the phase space

$$\bar{\Psi}_i(\mathbf{x}, t) = \frac{1}{n_i} \int \Psi f_i d\mathbf{c} dY_\xi dT dm \quad (3)$$

Here n_i denotes the number density of the solid class i , and is defined as

$$n_i(\mathbf{x}, t) = \int f_i d\mathbf{c} dY_\xi dT dm \quad (4)$$

It is also convenient to introduce mass-weighted averages

$$\bar{\Psi}_i(\mathbf{x}, t) = \frac{1}{\alpha_i \bar{\rho}_i} \int m_i \Psi f_i d\mathbf{c} dY_\xi dT dm \quad (5)$$

where $\alpha_i \bar{\rho}_i = n_i \bar{m}_i = \int m_i f_i d\mathbf{c} dY_\xi dT dm$. This definition of the mass-weighted particle average is completely comparable to that used for the carrier phase and leads to more convenient forms of the macroscopic equations (see below).

Here, α_i denotes the local phase fraction of class i (where pores are excluded, i.e., are counted as part of the gas phase) and $\bar{\rho}_i$ its corresponding average particle density. We also introduce equivalent definitions for $\hat{\alpha}_i$ and $\hat{\rho}_i$ where the pores of the particles are counted as volume belonging to the particle. Note that $\alpha_i \bar{\rho}_i = \hat{\alpha}_i \hat{\rho}_i$. Mass-weighted averages are also denoted by brackets, i.e., $\langle \Psi \rangle_i \equiv \bar{\Psi}_i$ in the equations below. Using the above definitions we define the average velocity $\mathbf{u}_i = \langle \mathbf{c} \rangle_i$, the fluctuation velocity component, $\mathbf{C}_i = \mathbf{c}_i - \mathbf{u}_i$, and the granular temperature, $\Theta_i = \frac{1}{3} \langle C_i^2 \rangle$. The granular temperature plays a crucial role in the determination of the transport properties of granular flows and may be interpreted similarly to the temperature of a normal gas (see, for example, Campbell⁸).

The solidity of a particle, $\eta = 1 - \epsilon$, where ϵ is the porosity of a particle, is defined as the ratio of the volume displaced by the particle and the volume displaced by the particle if its pores had been closed. The solidity is then easily shown to equal

$$\eta_i = \frac{m_i \sum Y_\xi}{V_i \rho_\xi} \quad (6)$$

where V_i is the total volume of a particle (including its pores). In the present case of biomass pyrolysis, we assume that the particle diameter stays constant throughout the pyrolysis, and that the porosity of the particle simply increases in time (Miller and Bellan⁴). This assumption is correct when the particle does not break or erodes.

2.2.2. Macroscopic Equations. Mass. The mass conservation equation for the gas phase is

$$\frac{\partial(\alpha \bar{\rho})_g}{\partial t} + \nabla \cdot (\alpha \bar{\rho} \mathbf{u})_g = \Gamma_g \quad (7)$$

where α , ρ , and \mathbf{u} denote the volume fraction, density, and velocity, respectively. The term on the right-hand side, Γ_g , represents the mass transfer rate originating from pyrolysis.

Similar equations can be derived for each solid class i through the formalism stated earlier:

$$\frac{\partial(\alpha \bar{\rho})_i}{\partial t} + \nabla \cdot (\alpha \bar{\rho} \mathbf{u})_i = \Gamma_i \quad (8)$$

where the mass transfer rate for each solid class is related to the average mass reduction of all particles in

(7) Drew, D. A. Mathematical modeling of two-phase flow. *Annu. Rev. Fluid Mech.* **1983**, *15*, 261–291.

(8) Campbell, C. S. Rapid granular flows. *Annu. Rev. Fluid Mech.* **1990**, *22*, 57–92.

the specific class, $\Gamma_i = \alpha_i \bar{\rho}_i <(1/m_i)(dm_i/dt)>$, which may in turn be related to the average conversion rate of solid to gas-phase reactions $\Gamma_i = \alpha_i \bar{\rho}_i \sum_{\xi} \langle R_{i,\xi} \rangle$, with $R_{i,\xi}$ denoting the total reaction rate for particle class i and species ξ . For inert particles, this term is absent. For consistency we require $\Gamma_g + \sum_i \Gamma_i = 0$.

Momentum. After some mathematical manipulations and modeling (see Lathouwers and Bellan⁶), the gas-phase momentum equation can be written as

$$\frac{\partial(\alpha \bar{\rho} \tilde{\mathbf{u}})_g}{\partial t} + \nabla \cdot (\alpha \bar{\rho} \tilde{\mathbf{u}} \tilde{\mathbf{u}})_g = -\alpha_g \nabla \bar{p}_g + \nabla \cdot 2\alpha_g \mu_g \mathbf{S}_g + \alpha_g \bar{\rho}_g \mathbf{f}_g + \sum_i \frac{\alpha_i \bar{\rho}_i}{\tau_{i,12}} (\mathbf{u}_i - \tilde{\mathbf{u}}_g) - \sum_i \Gamma_i \mathbf{u}_i \quad (9)$$

where p_g is the thermodynamic pressure, \mathbf{S}_g denotes the strain rate tensor $\mathbf{S}_g = (\nabla \tilde{\mathbf{u}}_g + \nabla \tilde{\mathbf{u}}_g^T)/2 - (\nabla \cdot \tilde{\mathbf{u}}_g)/3$, μ_g is the shear viscosity, \mathbf{f}_g is the gravitational acceleration, and $\tau_{i,12}$ is the fluid particle interaction time scale. The terms on the right-hand side denote the pressure gradient force, shear stresses, gravitational body force, the force exerted on the gas phase by drag on the particles, and finally, the effect of mass transfer on the momentum of the carrier gas.

The thermodynamic pressure, p_g , is related to the gas-phase temperature, T_g , and density, $\bar{\rho}_g$, through the average equation of state

$$\bar{p}_g = R_u \bar{\rho}_g \sum_{\xi} \frac{\bar{Y}_{\xi}}{W_{\xi}} \bar{T}_g \quad (10)$$

where R_u denotes the universal gas constant, and W_{ξ} is the molecular weight of species ξ .

The gas-particle interaction time scale, $\tau_{i,12}$, depends strongly on the flow regime; in the dilute regime it is derived from the drag coefficient, C_d , of a single particle in an infinite medium, empirically corrected for the presence of other surrounding particles by a function $f(\alpha_g) = \hat{\alpha}_g^{-1.7}$ (e.g., Gidaspow⁹) whereas in the dense regime the classical Ergun relation is used. To avoid discontinuous behavior, a weighted average of the two time scales is introduced:

$$\frac{1}{\tau_{i,12}} = \frac{3\bar{\rho}_g C_d(Re_i)}{4\bar{\rho}_i d_i} |\mathbf{u}_i - \tilde{\mathbf{u}}_g| f(\hat{\alpha}_g) + (1 - W) \frac{\bar{\rho}_g}{\bar{\rho}_i} \left[(1 - \hat{\alpha}_g) \frac{150}{Re_i} + 1.75 \right] \frac{|\mathbf{u}_i - \tilde{\mathbf{u}}_g|}{d_i} \quad (11)$$

where the present switch function, $W(\hat{\alpha}_g) = \arctan(150 - (\hat{\alpha}_g - 0.8))/\pi + 1/2$, gives a rapid transition from one regime to the other, d_i is the diameter of the particle, and Re_i is the Reynolds number based on the relative velocity with the gas, $Re_i = \hat{\alpha}_g \rho_g |\mathbf{u}_i - \tilde{\mathbf{u}}_g| d_i / \mu_g$. The single-particle drag coefficient C_d is determined from the well-known correlation (Schiller and Nauman¹⁰)

$$C_d = 24 Re_i (1 + 0.15 Re_i^{0.687}) \quad (12)$$

In the modeling of the momentum transfer associated with mass transfer from solid to gas phase, it has been assumed that fluctuations in the particle velocity are negligible.

The averaged momentum equation for each solids class is

$$\frac{\partial(\alpha \bar{\rho} \tilde{\mathbf{u}})_i}{\partial t} + \nabla \cdot (\alpha \bar{\rho} \tilde{\mathbf{u}} \tilde{\mathbf{u}})_i = -\hat{\alpha}_i \nabla \bar{p}_g - \nabla \cdot (\Sigma_i + \Sigma_i^f) + \alpha_i \bar{\rho}_i \mathbf{f}_g + \frac{\alpha_i \bar{\rho}_i}{\tau_{i,12}} (\tilde{\mathbf{u}}_g - \mathbf{u}_i) + \phi_i + \Gamma_i \mathbf{u}_i \quad (13)$$

This equation contains similar terms when compared to its gas-phase counterpart, i.e., a mean pressure gradient, a drag term having the reverse sign compared to that in the gas-phase equation, and a mass transfer related term. Terms unique to the solid's equation are the solid stress tensors, Σ_i and Σ_i^f , and a collisional source term, ϕ_i which represents the momentum exchange among the various solid classes due to collisions. Note, however, that both collisions between particles from the same class and collisions between particles from different classes contribute to Σ_i , while ϕ_i only contains contributions from collisions between unlike particles. Closure relations for these terms, derived by Lathouwers and Bellan,⁶ are provided below.

Collisional models determining Σ_i are restricted to the region where particles interact exclusively through slightly inelastic, short-duration collisions. However, as the volumetric fraction approaches the maximum packing volume fraction (i.e., in the dense particle packing regime), α_{max} , particles will, increasingly, be in simultaneous contact with several neighbors and stresses will be transmitted at points of sustained sliding or rolling contact. Considering the high particle volume fraction in a bubbling fluidized bed, the solid's momentum equations include a specific frictional stress term, Σ_i^f , that prevents the particles from overpacking even when collisions are absent (for vanishingly low granular temperature). The proposed model consists of a simple relationship between stresses and strains: $\Sigma_i^f = -p_i^f \mathbf{I} + 2\mu_i^f \mathbf{S}_i$ for $\alpha > \alpha_{min}$ where α_{min} is the minimum solids fraction at which frictional transfer becomes influential. Experimental observations indicate that the frictional normal stress increases rapidly with bulk density and diverges as α_{max} is approached. A simple algebraic representation of this behavior is (cf. Anderson and Jackson¹¹)

$$p_i^f = \frac{\alpha_i \rho_i}{\sum \alpha_j \rho_j} \text{Fr} \frac{(\hat{\alpha} - \alpha_{min})^p}{(\alpha_{max} - \hat{\alpha})^n} \quad (14)$$

where Fr is a material constant. The frictional viscosity, μ_i^f , is related to the frictional pressure and the angle of internal friction, ϕ , as $\mu_i^f = p_i^f \sin(\phi)/2\sqrt{I_2}$ where I_2 denotes the second invariant of the strain rate tensor. The following values for the parameters have been used in the present work: $p = 2$, $n = 5$, $\text{Fr} = 0.005$, $\alpha_{min} =$

(9) Gidaspow, D. Hydrodynamics of fluidization and heat transfer: supercomputer modelling. *Appl. Mech. Rev.* **1986**, 39, 1–22.

(10) Schiller, L.; Nauman, A. A drag coefficient correlation. *VDI Zeitung* **1935**, 77, 318–320.

(11) Anderson, K. G.; Jackson, R. A comparison of the solutions of some proposed equations of motion of granular materials for fully developed flow down inclined planes. *J. Fluid Mech.* **1992**, 241, 145–168.

0.6, $\alpha_{max} = 0.64$, and $\phi = 25$ degrees (see Lathouwers and Bellan⁵).

Species. Applying the averaging formalism to the gas-phase species equations, one obtains

$$\frac{\partial(\alpha\bar{\rho}\tilde{Y}_{\xi})_g}{\partial t} + \nabla \cdot (\alpha\bar{\rho}\mathbf{u}\tilde{Y}_{\xi})_g = \nabla \cdot \alpha_g\bar{\rho}_g\mathcal{D}_{\xi}\nabla\tilde{Y}_{\xi} + \alpha_g\bar{\rho}_g\tilde{R}_{\xi} + \sum_i \alpha_i\bar{\rho}_i\langle R_{i,\xi}^{s-g} \rangle \quad (15)$$

Here, we have neglected turbulent transport in the gas phase (see Lathouwers and Bellan¹² for an outline of a turbulence model). The first term on the right-hand side represents molecular diffusion and \mathcal{D}_{ξ} is the diffusion coefficient (multicomponent fluxes are neglected); the second term is the average production rate of species ξ due to gas-phase reaction; whereas the final term denotes the mass source for a particular component due to solid's reactions, converting solids to gas.

For the species in each solid class, a similar equation is obtained

$$\frac{\partial(\alpha\bar{\rho}\tilde{Y}_{\xi})_i}{\partial t} + \nabla \cdot (\alpha\bar{\rho}\mathbf{u}\tilde{Y}_{\xi})_i = \nabla \cdot (\alpha_i\bar{\rho}_i\mathcal{D}_{ii}\nabla\tilde{Y}_{\xi}) + \Gamma_{i,\xi} \quad (16)$$

The first term on the right-hand side denotes the diffusion of species due to fluctuations in the velocity of the solids. \mathcal{D}_{ii} is calculated as the self-diffusion coefficient which is directly derived from the velocity distribution of the particles (see Lathouwers and Bellan⁶ for a detailed derivation). The second term, $\Gamma_{i,\xi} = \alpha_i\bar{\rho}_i\langle R_{i,\xi} \rangle$ is the average mass source arising from the pyrolysis reactions.

Thermal Energy. The thermal energy equation for the gas phase is

$$(\alpha\bar{\rho}C_p)_g \frac{D_g\tilde{T}_g}{Dt} = \nabla \cdot \alpha_g\lambda_g\nabla\tilde{T}_g + \sum_i \frac{6\hat{\alpha}_i\lambda_g}{d_i^2} \text{Nu}_i(\tilde{T}_i - \tilde{T}_g) + \sum_i \{ \Gamma_{tar}^{s-g}(C_p^{tar}\tilde{T}_b - C_{p,g}\tilde{T}_g) + \Gamma_{gas}^{s-g}(C_p^{gas}\tilde{T}_i - C_{p,g}\tilde{T}_g) \} \quad (17)$$

The first term on the right-hand side is the thermal conductive flux where λ_g is the thermal conductivity. The second term represents the heat exchange with the particles by conduction and convection; Nu_i denotes the effective Nusselt number associated with this transfer. The final collection of terms is the excess enthalpy flux entering the gas-phase carried by the gaseous products leaving the particles, where it is assumed that the vapor products leave the particle at its mean temperature. Γ_{tar}^{s-g} and Γ_{gas}^{s-g} denote the averaged mass transfer rates of, respectively, tar and gas. More details concerning the derivation of the latter term are given in Lathouwers and Bellan.⁶

In obtaining relevant Nusselt relations for this situation, it is assumed that the particle temperature is uniform, i.e., the resistance to heat transfer is mainly in the gas phase. This assumption is consistent with those used to derive the continuum theory, as the state variables of the particles include their mean temperature only, i.e., no information on the internal temperature distribution is available. Implicitly, the Biot numbers are assumed small ($\text{Bi} = h_id/\lambda_b$, where h_i is the gas-particle heat transfer coefficient). In the present

case, the Nusselt number is given by the single-particle Nusselt relation, multiplied by a correction factor, F_{bh} , accounting for the effect of mass transfer on the heat transfer rate, i.e.,

$$\text{Nu} = \text{Nu}_0 F_{bh}(\text{Re}_{bh}, \text{Pr}_g) \quad (18)$$

The formulation used here for the blowing factor is that taken from Miller et al.¹³ and was also given by Gyarmathy¹⁴ where the factor depends on the "blowing Reynolds number", $\text{Re}_{bh} = \dot{m}/\pi d\mu_g$,

$$F_{bh} = \frac{\text{Pr}_g \text{Re}_{bh}/2}{e^{\text{Pr}_g \text{Re}_{bh}/2} - 1} \quad (19)$$

To calculate Nu_0 , we use the standard Ranz correlation

$$\text{Nu}_0 = 2 + 0.66\text{Re}_i^{1/2} \text{Pr}_g^{1/3} \quad (20)$$

The final enthalpy equation for each solid class is

$$(\alpha\bar{\rho}C_p)_i \frac{D_i\tilde{T}_i}{Dt} = \nabla \cdot (\alpha_i\bar{\rho}_iC_{p,i}\mathcal{D}_{ii}\nabla\tilde{T}_i) + \frac{6\hat{\alpha}_i\lambda_g}{d_i^2} \text{Nu}_i(\tilde{T}_g - \tilde{T}_i) + \alpha_i\bar{\rho}_i\langle Q_{r,i}/m_i \rangle + \alpha_i\bar{\rho}_i\langle (dm/d\dot{t})(h_v - \tilde{h}_i)/m_i \rangle \quad (21)$$

As in the case of the solid species equations, the diffusive transport of heat has been modeled through a self-diffusion coefficient. The second term on the right-hand side is also present in the gas-phase equation, and was discussed above. The term $\alpha_i\bar{\rho}_i\langle Q_{r,i}/m_i \rangle$ denotes the source due to thermal radiation processes. A similar term is not present in the gas-phase equation because at the temperatures of interest, the gas may be considered transparent. This radiative source is modeled through knowledge of the absorptivity, κ_{ai} , and of the radiation intensity within the domain. In the present model, the radiation intensity is calculated on the basis of a six-flux method; more details may be found in Lathouwers and Bellan.⁶ With the calculated radiative intensities, the sources in the thermal energy equations of the solids are given by

$$\alpha_i\bar{\rho}_i \left\langle \frac{Q_{r,i}}{m_i} \right\rangle = -4\pi\kappa_{ai} \left(I_{bbi} - \frac{I_x + I_y + I_z}{3} \right) \quad (22)$$

with the blackbody intensity for class i given by $I_{bbi} = \sigma_B T_i^4/\pi$ where σ_B is the Stefan Boltzmann constant. The absorption and scattering coefficients (required within the six-flux method) are calculated in the optical limit where the efficiency factors for absorption and scattering equal unity, i.e.,

(12) Lathouwers, D.; Bellan, J. Multiphase flow equations for modeling tar production from biomass particle pyrolysis in a fluidized bed reactor. Fall Technical Meeting of the Western States Section of the Combustion Institute, Irvine, October 25–26, 1999.

(13) Miller, R. S.; Harstad, K.; Bellan, J. Evaluation of equilibrium and nonequilibrium evaporation models for many-droplet gas-liquid flow simulations. *Int. J. Multiphase Flow* **1999**, *24* (6), 1025–1055.

(14) Gyarmathy, G. The spherical droplet in gaseous carrier streams: review and synthesis. *Multiphase Science and Technology*; Hewitt, G. F., Delhay, J. M., Zuber, N., Eds.; McGraw Hill: New York, 1982; Vol. 1, pp 99–279.

$$\kappa_{ai} = \kappa_{si} = \frac{3}{2} \frac{\hat{\alpha}_i}{d_i} \quad (23)$$

The final term on the right-hand side of eq 21 is exactly equal to the total average heat of reaction of all reactions taking place in the particle (both solid to solid and solid to gas).

Granular Kinetic Energy. The transport equation for the granular temperature of each particle class is

$$\frac{3}{2} \left[\frac{\partial(\alpha \bar{\rho} \Theta)_i}{\partial t} + \nabla \cdot (\alpha \bar{\rho} \tilde{\mathbf{u}} \Theta)_i \right] = -\Sigma_i \cdot \nabla \tilde{\mathbf{u}}_i - \nabla \cdot \mathbf{q}_i + \gamma_i + \frac{3}{2} \Gamma_i \Theta_i \quad (24)$$

The first term on the right-hand side of eq 24 is the production of kinetic energy of the fluctuations due to shearing of the solid phase. Note, however, that only collisional stresses contribute to this term whereas frictional terms are deleted, inherently assuming that the frictional work is directly converted to thermal internal energy. \mathbf{q}_i is the average “heat flux” both due fluctuations in the velocity of the particles and through collisions. Both like and unlike particle collisions contribute to this flux. The source term, γ_i , represents the effects of energy redistribution among particle classes and the dissipative effect of inelastic collisions. This term is also composed of contributions between like and unlike particles. The effect of mass transfer is contained in the last term of eq 24. The effects of the carrier gas have been neglected in this equation, which is warranted by the fact that the particles of interest are relatively heavy. That is, velocity fluctuations in the gas phase do not affect the particle velocity too strongly. Furthermore, in the dense systems here of interest, the fluid mechanics is dominated by collisional effects, not by the turbulence of the carrier gas. Closure for the collisional source and flux are provided below.

Collisional and Kinetic Contributions. The above model describes a particle mixture in a gaseous carrier using conservation equations for mass, momentum energy, and granular temperature of each solid class. These multiple-class equations describe the independent accelerations of the species, as well as momentum and energy exchange between solid classes. Several terms in the transport equations have already been modeled, such as transfer-related terms. We have purposely left other terms in the equations so far unspecified in order to discuss their origin and closure. Specifically, collisional and kinetic sources and fluxes and their related transport properties are discussed in the present section.

In principle, the single-particle distribution functions are solutions of Boltzmann-type equations; however, they are difficult to obtain in situations when the phase space includes many variables (mass fractions, temperature, etc.). Therefore, it has been assumed that the velocity distribution function for solution of the hydrodynamic problem can be obtained without incorporating the explicit effect of the thermochemistry. The hydrodynamic problem is then basically decoupled from the thermochemistry as far as the velocity distribution is concerned, and the velocity distributions may be obtained by similar techniques as are used in a nonreac-

tive flow, taking into account the mean evolution of, for instance, the particle mass.

Therefore, the single particle distribution function is assumed to be Maxwellian, i.e., the lowest order approximation to the Boltzmann equation in the absence of dissipative effects:

$$f_i^{(1)}(\mathbf{x}, \mathbf{c}_i, t) = \frac{n_i}{(2\pi\Theta_i)^{3/2}} \exp \left[\frac{-(\mathbf{c}_i - \tilde{\mathbf{u}}_i)^2}{2\Theta_i} \right] \quad (25)$$

This is a good approximation when the flow has small spatial gradients, the collisions are nearly elastic and the particles are sufficiently heavy (i.e., the time between collisions is much smaller than the particle relaxation time; the particle–fluid correlation is small). The integrals require specification of the radial distribution function at contact, $h_{ik}(\mathbf{r})$, accounting for the effects of excluded area and particle shielding on the spatial distribution of colliding pairs. The form of the radial distribution function is taken from Jenkins and Mancini,¹⁵ slightly adjusted to prevent overpacking of the solids, α_{max} being the maximum allowable solids volume fraction

$$h_{ik} = \frac{1}{1 - \hat{\alpha}/\alpha_{max}} + 6 \frac{\sigma_i \sigma_k}{\sigma_i + \sigma_k (1 - \alpha/\alpha_{max})^2} + 8 \left(\frac{\sigma_i \sigma_k}{\sigma_i + \sigma_k} \right)^2 \frac{\xi}{(1 - \hat{\alpha}/\alpha_{max})^3} \quad (26)$$

Here, $\xi = 2\pi/3 \sum n_i \sigma_i^2$ where σ_i denotes the radius of a particle of class i .

The present study is targeted toward dense systems where the drift between particle classes is small. Therefore, the collision integrals are approximated by assuming that the relative velocity $\Delta \mathbf{u}_{ik} = \mathbf{u}_i - \mathbf{u}_k$, is small compared to the square root of the sum of the granular temperatures, $(\Theta_i + \Theta_k)^{1/2}$. This significantly simplifies the calculation of the required integrals, and furthermore should not affect the applicability of the equations for our purposes. A more detailed discussion may be found in Lathouwers and Bellan.⁶

Using the above distributions and neglecting products of the spatial gradients, products of $(1 - e_{ik})$ with spatial gradients, and products of $\Delta \mathbf{u}_{ik}$ with the spatial gradients, yields the following constitutive equations for ϕ_i , Σ_i , \mathbf{q}_i , and γ_i :

$$\phi_i = \sum_k F_{ik} \left\{ \frac{4}{3} \sqrt{2\pi(\Theta_i + \Theta_k)^{1/2}} (\tilde{\mathbf{u}}_k - \tilde{\mathbf{u}}_i) + \frac{\pi}{3} \sigma_{ik} (\Theta_i + \Theta_k) \nabla \ln \frac{n_i}{n_k} \right\} \quad (27)$$

$$\Sigma_i = n_i m_i \Theta_i \mathbf{I} + \sum_k \left\{ p_{ik} \mathbf{I} - \mu_i^{ik} \left[2\mathbf{S}_i + \frac{5}{3} \nabla \cdot \tilde{\mathbf{u}}_i \right] - \mu_i^{kk} \left[2\mathbf{S}_k + \frac{5}{3} \nabla \cdot \tilde{\mathbf{u}}_k \right] \right\} \quad (28)$$

(15) Jenkins, J. T.; Mancini, F. Balance laws and constitutive relations for plane flows of a dense, binary mixture of smooth, nearly elastic, circular disks. *J. Appl. Mech.* **1987**, *54*, 27–34.

$$\mathbf{q}_i = \sum_k \{ \kappa_i^{ik} \nabla \Theta_i + \kappa_i^{kk} \nabla \Theta_k \} \quad (29)$$

$$\gamma_i = \sum_k -2\sqrt{2\pi} F_{ik} (\Theta_i + \Theta_k)^{1/2} \{ 2(M_i \Theta_i - M_k \Theta_k) + M_k(1 - e_{ik})(\Theta_i + \Theta_k) \} \quad (30)$$

where $F_{ik} = n_i n_k m_i M_k (1 + e_{ik}) h_{ik} \sigma_{ik}^2$. The indices on the viscosities and conductivities are arranged as follows: the subscript i indicates the relevance for class i , the first superscript labels the pertinent velocity gradient, and the k superscript denotes the collisions with particles from class k . The pressure and transport coefficients are

$$p_{ik} = \frac{1}{3} \pi n_i n_k m_i M_k (1 + e_{ik}) h_{ik} \sigma_{ik}^3 (\Theta_i + \Theta_k) \quad (31)$$

$$\mu_i^{ik} = \frac{1}{15} \sqrt{2\pi} n_i n_k m_i M_k^2 (1 + e_{ik}) h_{ik} \sigma_{ik}^4 (\Theta_i + \Theta_k)^{3/2} / \Theta_i \quad (32)$$

$$\mu_i^{kk} = \frac{1}{15} \sqrt{2\pi} n_i n_k m_k M_k^2 (1 + e_{ik}) h_{ik} \sigma_{ik}^4 (\Theta_i + \Theta_k)^{3/2} / \Theta_k \quad (33)$$

$$\kappa_i^{ik} = \frac{1}{3} \sqrt{2\pi} n_i n_k m_i M_k (1 + e_{ik}) h_{ik} \sigma_{ik}^4 (\Theta_i + \Theta_k)^{1/2} (M_k \Theta_k / \Theta_i) \quad (34)$$

$$\kappa_i^{kk} = \frac{1}{3} \sqrt{2\pi} n_i n_k m_k M_k (1 + e_{ik}) h_{ik} \sigma_{ik}^4 (\Theta_i + \Theta_k)^{1/2} (M_i \Theta_i / \Theta_k) \quad (35)$$

The terms in ϕ_i represent solid–solid drag and ordinary diffusion, respectively (thermal diffusion has been neglected). The stress tensor depends on the shear rates of all solid classes where the shear viscosities arise entirely from collisions, not from streaming; this is a result of the Gaussian approximation. Similar remarks hold for the heat flux vector. Recently, Manger¹⁶ has presented similar closure relations for binary mixtures. For coding purposes, the shear rates of both phases are assumed equal (small drift) so that the actually used viscosity equals the sum of several contributions: $\mu_i = \sum_k \mu_i^{ik} + \mu_i^{kk}$. A similar procedure has been used for the conductivity. This procedure renders the resulting equations coupled only through algebraic, rather than also differential, terms and thus makes the code more computationally efficient.

Auxiliary Relations. The hydrodynamics of the system strongly depends on the mass of the particles in each class. Very light particles, for example, tend to be blown out of the bed by the carrier gas while heavier particles are more difficult to fluidize. Due to solid conversion to gaseous products, the mass of biomass particles decreases as time progresses. Therefore, one must simultaneously consider both freshly fed biomass as well as fully converted, nonreactive waste particles. To account for this spatial-temporal effect, the following transport

equation for the mean particle mass of each reactive solid is solved:

$$\frac{\partial(\alpha \bar{\rho} \bar{m})_i}{\partial t} + \nabla \cdot (\alpha \bar{\rho} \bar{\mathbf{u}} \bar{m})_i = \nabla \cdot (\alpha \bar{\rho}_i \mathcal{D}_{ii} \nabla \bar{m}_i) - 2\Gamma_i \bar{m}_i \quad (36)$$

This equation states that mass is convected along the mean velocity while mass transfer effects portrayed by the final term in the equation, cause a reduction in the mass. The diffusion term is analogous to those already encountered in the species and energy equations and reflects the effect of velocity fluctuations on the mixing of the solids.

In the above model, conversion of α_i to $\hat{\alpha}_i$ and vice versa is performed through knowledge of the solidity of the porous particles which can be related to the average species mass, \bar{m}_i , the particle volume, V_i (considered constant), and its composition

$$\bar{\eta}_i = \frac{\bar{m}_i}{V_i} \sum_{\xi} \frac{\bar{Y}_{\xi}}{\rho_{\xi}} \quad (37)$$

The model contains many average reactive sources. These averages are all evaluated at the average temperature and mass fractions. For example, the mass exchange rate is evaluated as

$$\Gamma_i = \alpha \bar{\rho}_i \sum_{\xi} \bar{R}_{i,\xi}^{s \rightarrow g} = \alpha \bar{\rho}_i \sum_{\xi} R_{i,\xi}(\{ \bar{Y} \}, \bar{T}_i) \quad (38)$$

where $\{ \bar{Y} \}$ denotes any pertinent combination of the set of species mass fractions and where only solid-to-gas reactions need to be considered. Although this procedure neglects correlations between particle temperature and the mass fractions, these approximations are not very restrictive since the reaction rates are first order with respect to the species, and therefore do not exhibit the stronger nonlinearity normally associated with second or higher order reaction rates.

Finally, transport properties are required, such as the specific heats (both gas and solids) and thermal conductivities (gas only). These are calculated from a mass-weighted average of the individual species properties. Considering ϕ to be one such general property, its average is then computed from $\bar{\phi} = \sum_{\xi} Y_{\xi} \phi_{\xi}$. An exception to this procedure is in the calculation of the average particle density, $1/\bar{\rho}_i = \sum_{\xi} Y_{i,\xi} \rho_{\xi}$.

2.3. Initial and Boundary Conditions. Initial conditions are specified corresponding to the standard fluid bed shown in Figure 1. The fluid bed is initially at rest, having specified the velocities of all phases to be null; the granular energy is set to a small number, typically $10^{-7} \text{ m}^2/\text{s}^2$. To induce bubbling, several void areas are created at the bottom of the bed by setting the void fraction to unity in specified computational cells. Practically, there are three such regions distributed on the x axis, at locations corresponding to cells 5–7, 18–20, and 30–32. Areas are then created by making these regions 5 computational cells high in the y direction. The effects of the initial conditions survive a minute fraction of the total physical time and do not affect the statistical behavior of the fluid flow.

Inflow conditions are specified to reflect realistic conditions corresponding to bubbling fluidization; at inlet sections, the volume fractions and velocities are

(16) Manger, E. Modelling and simulation of gas/solids flow in curvilinear coordinates. Ph.D. Thesis, Telemark College, Norway, 1996.

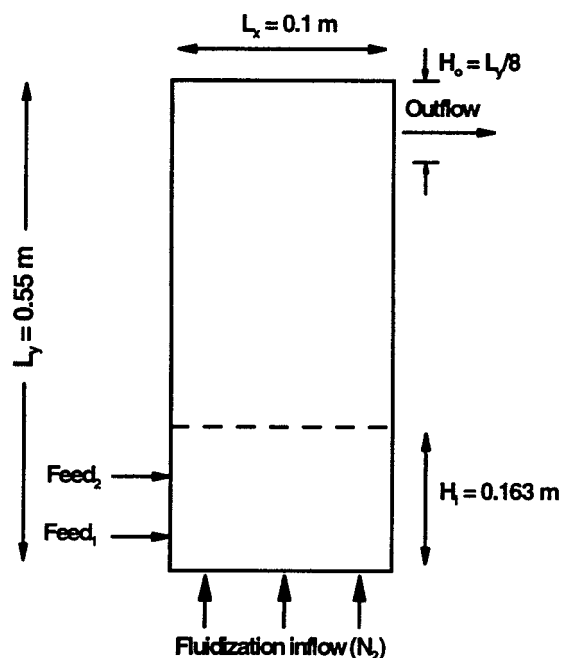


Figure 1. Schematic of the fluidized bed.

specified together with the temperatures of all phases and the composition of the gas phase and biomass particles, depending on the pertinent feedstock used. The initial temperature of both sand and gas in the domain is set equal to the inlet temperature of the fluidization gas. Hence, it is assumed that the fluidization gas has preheated the sand, even though initially the sand bed is stationary. This does not affect the calculation of product yield, as we are interested in the asymptotic (i.e., long time) behavior of the reactor; that is, long after which a statistically steady flow field has emerged.

Along solid walls, no-slip conditions are applied for the gas phase ($\vec{u}_g = 0$), whereas the solids are allowed to slip freely ($\partial \vec{u}_{s,t} / \partial n = 0$, where n is a unit normal and the subscript t denotes tangential). Zero-flux boundary conditions are imposed for the solids thermal energy equations, consistent with the energy transfer in particle-wall collisions being negligible. As the thermal boundary layers along the wall are not resolved, a similar condition is imposed for the gas phase. Boundary conditions for the thermal radiation model have been detailed by Zaichik et al.¹⁷ and have been stated in Lathouwers and Bellan⁶ for the specific application of the fluidized bed reactor.

At outlets, Neumann conditions are specified for all variables except for the velocity component normal to the outlet plane which is calculated using a prescribed atmospheric pressure at that plane. Solids are inhibited to exit the domain, simulating a fine solids-filtering grid.

3. Numerical Procedure

Spatial discretization of the governing equations is based on a finite volume technique using a staggered grid. All convective fluxes are approximated with a

second-order accurate bounded TVD-scheme avoiding the excessive numerical diffusion associated with the first-order accurate upwind scheme. The time discretization is based on a backward Euler scheme in combination with a pressure-correction technique with a time step adjustment procedure. The momentum equations of all phases are solved in a coupled manner, though separately for each velocity direction. Compared with the well-known Partial Elimination Algorithm (PEA), the present approach is more general (see Lathouwers¹⁸ for more details on full-field coupling and multiphase pressure correction algorithms). The species and energy equations constitute a strongly coupled, stiff system of equations. To avoid very large linear systems arising from (the necessarily) implicit discretization, a time splitting is used (Strang¹⁹) for the combined species and energy system consisting of three steps: (i) performance of a half convection-diffusion time step, (ii) time integration of the equations over a full time step with only the source terms present (reaction terms, radiation, etc.), (iii) performance of another half convection-diffusion time step. The advantage of this split scheme is that during steps (i) and (iii), the equations are decoupled into standard convection-diffusion systems which are easily handled, whereas in step (ii) there is no spatial coupling. The stiff integration in step (ii) is performed by using the well-known stiff integrator VODE (Brown et al.²⁰). All sparse linear systems arising from the discretization of convection-diffusion systems are solved with preconditioned Krylov methods (Conjugate Gradient (CG) for the pressure Poisson equation and Generalized Minimum RESidual (GMRES) for the other transport equations (e.g., Barrett et al.²¹)).

All computations have been performed on a 40×148 uniform grid (x and y directions, respectively). Runs have been performed in parallel (although the code is serial) on a SGI Origin 2000 supercomputer. Simulation of 5 s of physical time requires approximately 250 h of CPU time per run.

4. Biomass Particle Pyrolysis in a Fluidized Bed Reactor

Among the pyrolysis reactor designs investigated for commercial production of condensable tars from biomass, the fluidized bed reactor is potentially efficient due to the high particle heating rates that can be achieved (e.g., Scott et al.²²) and its excellent mixing properties, ensuring a reasonably uniform product quality. As stated above, a further interesting feature of this type of reactor is that char does not accumulate in the bed, but is elutriated with the gas flow instead, after which it may be filtered out, making the reactor very suitable for continuous operation.

(18) Lathouwers, D. Modelling and Simulation of Turbulent Bubbly Flows. Ph.D. Thesis, Delft University of Technology, The Netherlands, 1999.

(19) Strang, G. On the construction and comparison of difference schemes. *SIAM J. Numer. Anal.* **1968**, 5 (3), 506–517.

(20) Brown, P. N.; Byrne, G. D.; Hindmarsh, A. C. VODE: A Variable-coefficient ODE solver. *SIAM J. Sci. Stat. Comput.* **1989**, 10 (5), 1038–1051.

(21) Barrett, R.; Berry, M.; Chan, T. F.; Demmel, J.; Donato, J.; Dongarra, J.; Eijkhout, V.; Pozo, R.; Romine, C.; Van der Vorst, H. Templates for the solution of linear systems: building blocks for iterative methods. SIAM: Philadelphia, 1994.

(22) Scott, D. S.; Majerski, P.; Piskorz, J.; Radlein, D. A second look at fast pyrolysis of biomass – the RTI process. *J. Anal. Appl. Pyrolysis* **1999**, 51, 23–37.

(17) Zaichik, L. I.; Pershukov, V. A.; Kozelev, M. V.; Vinberg, A. A. Modeling of dynamics, heat transfer, and combustion in two-phase turbulent flows: 2. Flows with heat transfer and combustion. *Exp. Thermal Fluid Sci.* **1997**, 15, 311–322.

Table 1: Rate Constants and Activation Energy for the Biomass Pyrolysis Kinetics Scheme^a

reaction	A (1/s)	E (J/kmol)
K_1^c	2.8×10^{19}	242.4×10^6
K_2^c	3.28×10^{14}	196.5×10^6
K_3^c	1.30×10^{10}	150.5×10^6
K_1^h	2.10×10^{16}	186.7×10^6
K_2^h	8.75×10^{15}	202.4×10^6
K_3^h	2.60×10^{11}	145.7×10^6
K_1^l	9.60×10^8	107.6×10^6
K_2^l	1.50×10^9	143.8×10^6
K_3^l	7.70×10^6	111.4×10^6
K_4	4.28×10^6	108×10^6

^a The char formation ratios for reaction K_3 are $X^c = 0.35$, $X^h = 0.60$, and $X^l = 0.75$.

Table 2: Property Values for the Gas-Phase Species^a

species	W (kg/kmol)	C_p (J/kg K)	λ (J/ms K)	μ (kg/ms)	D (m ² /s)
N_2	28.013	1120.91	5.63×10^{-2}	3.58×10^{-5}	8.52×10^{-4}
gas	30	1100	2.577×10^{-2}	3.0×10^{-5}	1.1×10^{-4}
tar	100	2500	2.577×10^{-2}	3.0×10^{-5}	1.1×10^{-4}

^a The properties for nitrogen are taken at $T = 800$ K and $p = 100$ kPa.

Table 3: Specific Heat and Densities for Solid Species^a

species	C_p (J/kgK)	ρ (kg/m ³)
biomass	2300	2167
char	1100	2333
sand	800	2600

^a Biomass refers to both virgin species and active species.

Although the process has received considerable attention experimentally (e.g., Scott and Piskorz^{2,3}), currently there are no fundamental theoretical analyses available, addressing simultaneously all physicochemical processes in the reactor. Most of the work to date related to fluidized bed reactors has focused on single-particle pyrolysis in a gas stream which requires a priori knowledge of ambient gas flow parameters, its temperature in particular (Miller and Bellan,⁴ Di Felice et al.²³).

Below, we present quantitative results from numerical simulations based on the detailed mathematical model above, and we address the issues of tar collection efficiency and the potential for scale-up of the process.

4.1. Detailed Physicochemical Parameters of Biomass Pyrolysis. The kinetics scheme of the present biomass pyrolysis model was already presented in Section 2. All of the preexponential constants, A , and the reaction's activation energy, E , are tabulated in Table 1 (cf. Miller and Bellan⁴) and are dependent on the source component. Due to a lack of more detailed knowledge, the heats of reaction are taken as independent of the source component. The depolymerization reaction K_1 has $\Delta h_1 = 0$ kJ/kg, reaction K_2 is endothermic with $\Delta h_2 = 255$ kJ/kg, and both the char formation and the secondary tar reactions are exothermic with $\Delta h_3 = -20$ kJ/kg and $\Delta h_4 = -42$ kJ/kg. All other properties of gaseous and solid species are listed in Tables 2 and 3, respectively.

4.2. Simulation Details. A sketch of the simulated geometry and the standard dimensions employed is

Table 4: Initial Biomass Composition by Mass Fractions (see Miller and Bellan, 1997)

feed	cellulose	hemicellulose	lignin
bagasse	0.36	0.47	0.17
maple	0.40	0.38	0.22
olive husk	0.22	0.33	0.45
oak	0.35	0.40	0.25

given in Figure 1. The reactor standard size is $0.1 \text{ m} \times 0.55 \text{ m}$, and it is filled with sand only up to a height of 0.163 m at a volume fraction of 0.6 which corresponds to dense packing. The geometry has been chosen to resemble that used in experiments by Scott and Piskorz,^{2,3} among others. Although the real fluidized bed is a cylindrical vessel, for computational simplicity, the present computational domain is approximated to be rectangular. In the simulations, the biomass is fed through an inlet section in one of the side walls, together with an amount of gas, which preheats the biomass during the feeding process. The center of feed point 1 is located 4.6 cm from the bottom of the bed and has a height (area) of 1.86 cm ; feeder no. 2 has the same height (area) and is located 12.1 cm from the bottom. In the present simulations, the temperature of the gas used for fluidization, T_g , is equal to that fed through the biomass feed section; the inlet temperature of the biomass, T_b , however is assumed to vary in order to investigate the effect of biomass preheating. Note that, regardless of the biomass feed temperature, the biomass compositions used at the inlet correspond to those of biomass that has not pyrolyzed, i.e., it is assumed that the residence time in the feeder is short (no appreciable biomass conversion) while the effective heating of the particles is as efficient as required (by specifying the required temperature). To vary the cellulose/hemicellulose/lignin proportions of the feedstock, bagasse, olive husk, maple, and oak are used in the simulations. The initial biomass composition of these biomass types are given in Table 4. To investigate scale-up of the system, both proportional scaling and nonproportionally scaled fluidized beds have been explored. A summary of all simulations performed is listed in Table 5.

The diameter of the sand and biomass particles is varied from 0.5 to 1.0 mm , which are common values in practical operation. Biomass particles are assumed to have an initial porosity of 0.7 (cf. Miller and Bellan⁴) and the biomass feed flux is constant and has a value of $0.5 \text{ kg m}^{-2} \text{ s}^{-1}$ (when two feed points are used, the flow is equally split between feed points). The gas velocity through the feeder is 0.5 m/s , while the gas flow used for fluidization of the mixture is varied from 0.5 to 0.7 m/s and is uniform over the bottom of the domain.

4.3. Tar Collection Efficiency Parameters. The true measure of the reactor efficiency for the tar production can be quantitatively determined by comparing global quantities such as the actual mass of tar exiting the reactor (Ω_{tar}) and the amount still present in its interior (M_{tar}) to the biomass feed flow (M_{feed}):

$$\Omega_{tar} = \int_0^t \int_{outlet} (\alpha_g \rho_g \mathbf{u}_g Y_{tar}) \cdot \mathbf{dA} dt' \quad (39)$$

$$M_{tar} = \int_{reactor} (\alpha_g \rho_g Y_{tar}) dV \quad (40)$$

$$M_{feed} = \int_0^t \int_{inlet} (\alpha_b \rho_b \mathbf{u}_b) \cdot \mathbf{dA} dt' \quad (41)$$

(23) Di Felice, R.; Coppola, G.; Rapagna, S.; Jand, N. Modeling of biomass devolatilization in a fluidized bed reactor. *Can. J. Chem. Eng.* **1999**, *77*, 325–332.

Table 5: Summary of Operating Parameters in the Simulations Performed^a

run no.	T_g (K)	T_b (K)	feed-point	feed-stock	feed-rate	V_g (m/s)	d_p (mm)	scale-factor	radiation
0	750	400	1	bagasse	1	0.5	0.5	1	excl.
1	600	400	1	bagasse	1	0.5	0.5	1	incl.
2	700	400	1	bagasse	1	0.5	0.5	1	incl.
3*	750	400	1	bagasse	1	0.5	0.5	1	incl.
4	800	400	1	bagasse	1	0.5	0.5	1	incl.
5	850	400	1	bagasse	1	0.5	0.5	1	incl.
6	950	400	1	bagasse	1	0.5	0.5	1	incl.
7	750	450	1	bagasse	1	0.5	0.5	1	incl.
8	750	500	1	bagasse	1	0.5	0.5	1	incl.
9	750	400	1	bagasse	1	0.6	0.5	1	incl.
10	750	400	1	bagasse	1	0.7	0.5	1	incl.
11	750	400	1	olive husk	1	0.5	0.5	1	incl.
12	750	400	1	maple	1	0.5	0.5	1	incl.
13	750	400	1	oak	1	0.5	0.5	1	incl.
14	750	400	2	bagasse	1	0.5	0.5	1	incl.
15	750	400	1+2	bagasse	1	0.5	0.5	1	incl.
16	750	400	1	bagasse	1	0.5	0.75	1	incl.
17	750	400	1	bagasse	1	0.5	1.0	1	incl.
18	750	400	1	bagasse	2	0.5	0.5	1	incl.
19	750	400	1	bagasse	3	0.5	0.5	1	incl.
20	750	400	1	bagasse	1	0.5	0.5	2 (pr.)	incl.
21	750	400	1	bagasse	1	0.5	0.5	3 (pr.)	incl.
22	750	400	1	bagasse	1	0.6	0.5	2 (pr.)	incl.
23	750	400	1	bagasse	1	0.7	0.5	2 (pr.)	incl.
24	750	400	1	bagasse	1	0.5	0.5	2 (non-pr.)	incl.
25	750	400	1	bagasse	1	0.5	0.5	3 (non-pr.)	incl.

^a The standard conditions are those of Run 3, denoted by a star.

where the subscript b denotes biomass. With these definitions, two measures for reactor performance are the yield (η) and the differential reactor efficiency (DRE), ϑ , cf. Miller and Bellan:¹

$$\eta_{tar}(t) = \frac{\Omega_{tar} + M_{tar}}{M_{feed}} \quad (42)$$

$$\vartheta_{tar}(t) = \frac{\Omega_{tar} + M_{tar}}{\sum_{\xi}(\Omega_{\xi} + M_{\xi})} \quad (43)$$

where the summation is over the species tar, gas, and char. These measures quantify the relative efficiency of reactor tar production relative to the biomass feed flow, and the relative proportion of tar produced compared to gas and char. Similar definitions are used for the reactor performance with respect to gas and char production.

The above two definitions of tar collection are strongly related in that their values converge at steady-state conditions (i.e., states reached at sufficiently long time after reactor start-up) under certain circumstances. If conditions in the reactor are such that the pyrolysis reaction rate is at least equal to the feed rate of biomass into the reactor (i.e., sufficiently high temperature), then both definitions lead to the same steady-state value. This can easily be shown by considering the denominators of eqs 42 and 43, M_{feed} and $\sum_{\xi}(\Omega_{\xi} + M_{\xi})$, respectively. In the limit, $t \rightarrow \infty$, the two terms can differ only by a small amount corresponding to the unreacted biomass, and hence the yield and DRE will have approximately the same value since the unreacted amount of biomass is negligible. However, if the pyrolysis rate is lower than the biomass feed rate (under sufficiently low operating temperatures), then the yield will be lower than the obtained DRE. Thus, the DRE is an upper limit for the yield obtained at complete steady-state. This relation between the two collection param-

eters is noteworthy as it turns out that the DRE reaches a steady-state value earlier than the corresponding yield parameter.

4.4. Results

The model presented in Section 2 is quite complex, and as stated in Section 3, computationally intensive. It is therefore of interest to examine the effect of simplifications that may be possible, thereby reducing the CPU time. Lathouwers and Bellan⁵ have already determined that the collisional and friction models are essential for quantitative predictions of the fluidized bed hydrodynamics. Miller and Bellan⁴ have determined that the biomass kinetics presented in Section 2.1 is the only one capable of accurate predictions for a wide range of operating conditions. The only model whose importance has not yet been evaluated in the context of fluidized bed reactors is that of the multi-particle radiation. Thus, we first assess here the difference between results of simulations with and without radiation. Once this issue is settled, we present a quantitative study of various effects on tar collection, focusing on the prediction of the steady-state yield. In particular, we investigate how the different operating parameters affect it, and whether scale-up has a negative influence on tar collection thus inhibiting commercial viability.

4.4.1. Effects of Thermal Radiation. As outlined in the modeling section, the mathematical model contains a description of thermal radiative transfer between the hot sand and the cooler biomass particles. Single biomass particle simulations present in the literature always take gas-particle radiation into account, although compared to the particle-particle radiation heat transfer one may doubt its importance at the relatively low reactor temperatures used in biomass pyrolysis. At these relatively low temperatures, neither the rotational nor the vibrational gas modes are excited, and the gas is basically transparent for thermal radiation.

To quantify the effects of including the particle-particle radiation model on the obtained tar collection, simulations have been performed with and without this model and the results are presented in Figure 2. Conditions of these simulations pertain to the standard Run 3. The indication from Figure 2a illustrating the tar yield is that there is a distinctive effect on the prediction of this important quantity. Although the results have not reached their steady-state values, considerable difference is expected in the predicted values. To further investigate this effect, Figures 2b and 2c show the distribution of the biomass temperature at 2.5 s after start-up plotted for the same contour levels. Although the differences are hard to quantify, in general the contours in Figure 2c are more confined to the inlet region, indicating shorter heat-up times due to additional heat transfer from the sand to the biomass. The conclusion is that the particle-particle radiation model must be included for accurate tar yield prediction.

4.4.2. Steady-State Tar Yield Prediction. In a commercial reactor operation, the main interest is in steady-state values of the tar collection parameters. As already explained, if the pyrolysis rate is high enough to keep up with the feed rate (as it does in all but the low-temperature cases), there is a correspondence between the steady-state yield and the steady-state DRE. It is,

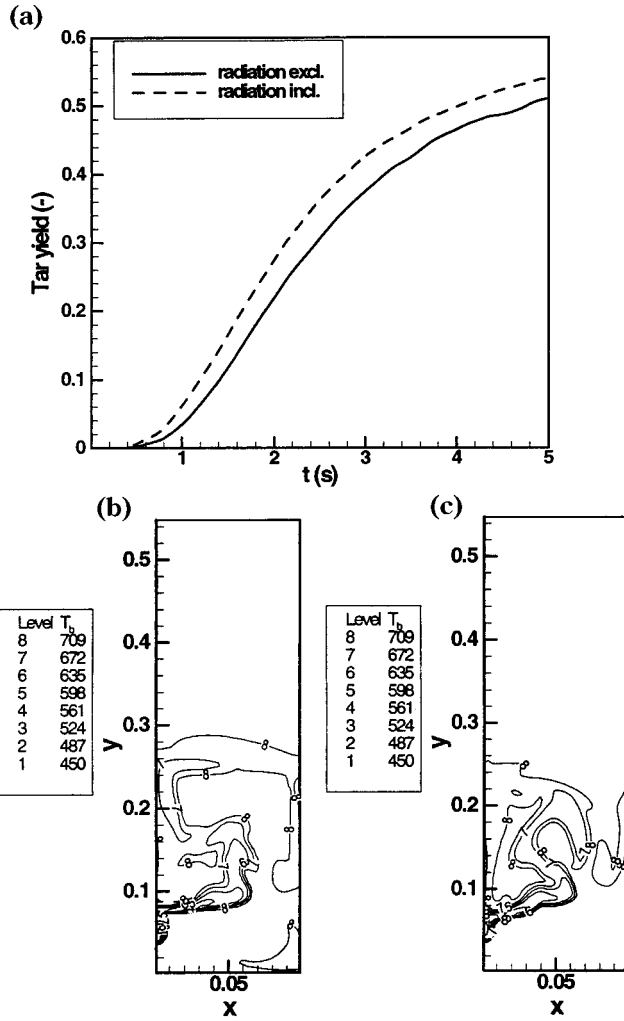


Figure 2. (a) Tar yield obtained from simulations with and without the radiation model, respectively, (b) biomass particle temperature at 2.5 s from a simulation without radiation taken into account, and (c) biomass particle temperature at 2.5 s taking radiation into account.

however, difficult to determine a priori whether for given conditions the DRE is an accurate representation of the tar yield. On the other hand, the present detailed simulations being computationally intensive, it is important to develop a strategy for predicting steady-state tar yield from short-time simulations. The idea here is to extrapolate the yield data in a meaningful manner. In fact, in cases where the temperature of the system is too low, and hence the reaction rate is slower than the feed rate, this is the only manner to obtain the steady-state values, as the DRE will constitute an over prediction in those situations, as discussed above. Notably, the yields approach their steady-state value approximately in an exponential way (see Lathouwers and Bellan⁶). Therefore, the yield data have been here fitted with an exponential function:

$$Y = Y_{\infty}(1 - e^{-\Psi}) \quad (44)$$

$$\Psi = \left(\frac{t - t_0}{\tau}\right)^s$$

where the parameters Y_{∞} , t_0 , τ , and s are to be determined by the fitting procedure, and Y_{∞} represents the

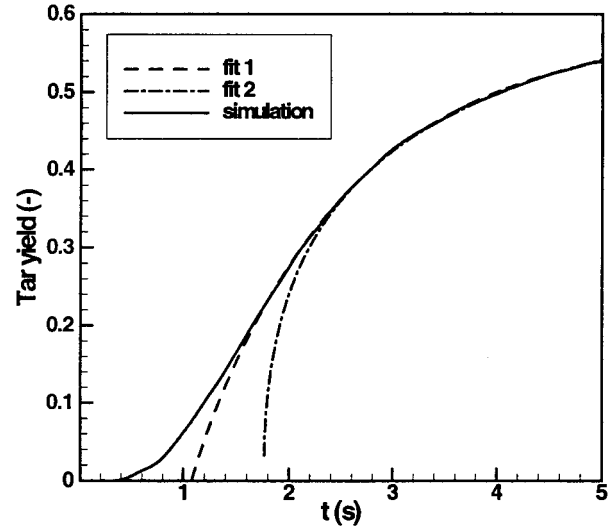


Figure 3. Example of the short-time tar-yield solution fits to obtain the steady-state tar yield. This tar yield solution was obtained for following initial conditions: $T_g = 750$ K, $T_b = 400$ K, $V_g = 0.5$ m/s, biomass particle diameter of 0.5 mm, and bagasse feedstock.

steady-state yield whose prediction is the present goal. The yield data are fitted over a time range, from the start time, t_s to the final 5 s. The start time is varied from 1 to 2.2 s, between which the yield starts to rise significantly. For each choice of start time, an optimal set of fit parameters is obtained (for Y_{∞} , t_0 , τ , and s). However, there are two primary uncertainties associated with this extrapolation process: (i) the yield may not be completely exponential, and (ii) the variation of the Y_{∞} for different choices of the start time, t_s may introduce uncertainties in the prediction. To illustrate the effect of a different choice of t_s , Figure 3 shows the tar yield as a function of time obtained from the standard simulation (Run 3) and 2 exponential fits with different t_s values. Although both fits appear to fit the data well in the intended region, their values of the steady-state tar yield differ significantly (fit 1: $Y_{\infty} = 0.585$; fit 2: $Y_{\infty} = 0.705$). In the subsequent parametric study, these uncertainties are denoted with error bars. We, however, emphasize that the existing uncertainty is not a major issue, as in most cases the DRE at 5 s may be approximately equated to the steady-state yield (except for the lower gas temperatures, or large particles).

4.4.3. Parametric Study. The effect of the most important process parameters determining the obtainable tar collection is here evaluated.

Displayed in Figure 4a is the yield at 5 s, the extrapolated yield, and the DRE, all for the tar, as a function of the gas temperature. Clearly there is an optimum in all curves at around 750 K. This temperature is in accordance with experimental data (e.g., Scott et al.²²) but the exact value of the optimum will depend on the type of biomass used. Noteworthy is the coincidence of the yield, extrapolated yield and the DRE at the highest temperatures, which is consistent with the fact that for these conditions the yield at 5 s appears to be almost steady (see Lathouwers and Bellan⁶). This coincidence gives confidence that the fitting procedure is valid. For the lower temperatures, the correspondence between the extrapolated yield and the DRE is still

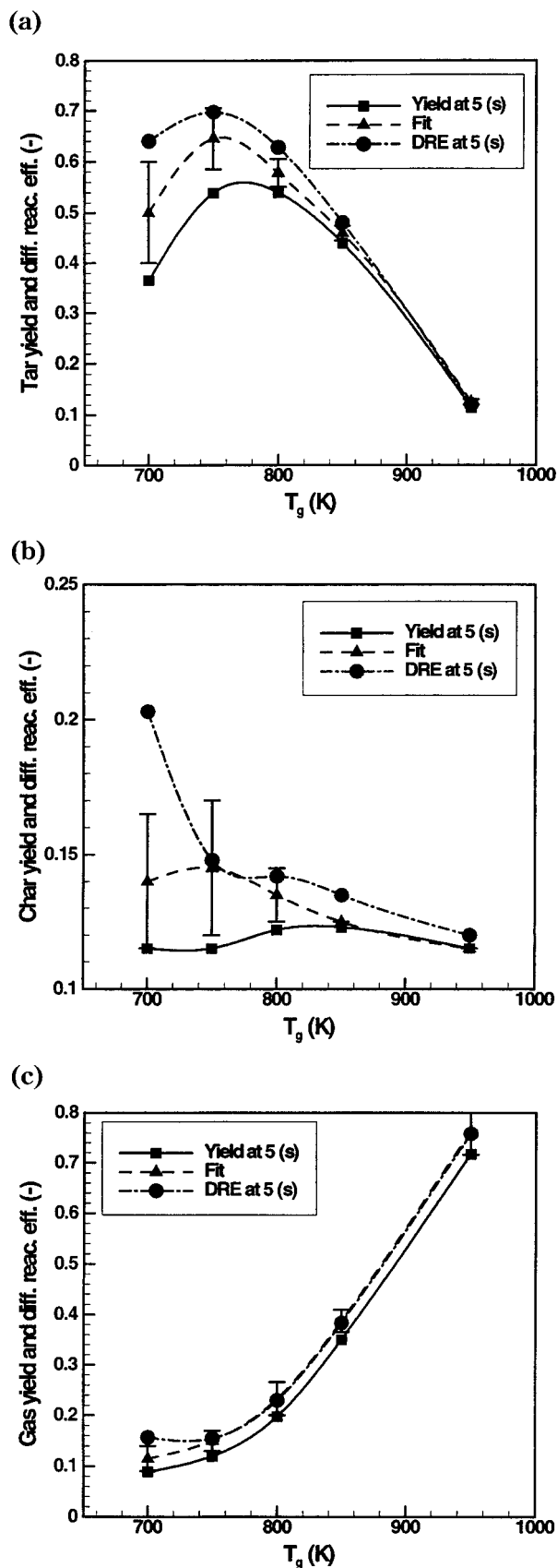


Figure 4. (a) Tar DRE, yield at 5 s, and predicted steady-state tar yield as a function of the fluidization gas temperature, (b) char DRE, yield, at 5 s and predicted steady-state char yield as a function of the fluidization gas temperature, and (c) gas DER, yield at 5 s, and predicted steady-state gas yield as a function of the fluidization gas temperature.

good, indicating that the extrapolation process is reasonable. Figure 4b shows similar results for char collection parameters. The general trend is that char collection decreases as the operating temperature increases. At lower temperatures the correspondence between the extrapolated char yield and the corresponding DRE is flawed. This may be due to the fact that in this case the char yield is not exponential as a function of time, with accompanying uncertainties in the fitting process. Figure 4c shows that, as the temperature is increased, the gas formation becomes dominant (cf. Miller and Bellan;¹ Di Felice²³).

Figure 5, parts a, b, and c, show the effect of the biomass feed temperature, the fluidization velocity, and the biomass feed rate, respectively. The effects of these parameters on tar collection are found to be relatively mild, as the slowest time is that of tar formation, which therefore governs the process. The figures do again indicate that in general the extrapolated yields are underpredicted compared to the DRE. The insensitivity of the short-time tar yield and the DRE to the feed rate, combined with the timewise evolution up to 5 s shown by Lathouwers and Bellan,⁶ represents strong evidence that at these conditions the tar reactions keep up with the feed rate, and therefore that the DRE is a good estimate of the steady-state tar yield. This observation is particularly important when discussing reactor scale-up.

The effect of biomass particle diameter variation is illustrated in Figure 5d. Note that no extrapolated values are shown as the curves were found to be far from steady-state (even the DRE values are not steady). The tar collection decreases strongly with the particle diameter due to a strong increase in the heat-up time of the particles. However, at steady-state it is expected that the weaker dependence displayed by the DRE will prevail. Nevertheless, for commercial operation, the particle diameter should be small so as to reduce heat-up times.

In Figure 5e the tar collection is depicted as function of the cellulose content of the biomass feed. The simulations exhibit a slight trend showing that tar collection increases with the cellulose percentage, similarly to the previous results of Miller and Bellan.⁴ Lathouwers and Bellan⁵ found that contrary to the accepted notion that the tar yield correlates positively with the percent cellulose, it seems to better correlate negatively with the percent lignin, indicating the importance of char formation reactions.

The relationship between biomass lignin content and char yield is displayed in Figure 6 showing both the char yield and DRE as function of the biomass lignin percentage for the four feedstocks used. The slight reduction for maple indicates that char formation is not only the result of lignin content, but is also intimately related to the process parameters, notably the gas temperature and heat up time. However, the general idea that char formation increases with lignin content seems to be confirmed.

4.4.4. Scale-up. As discussed above, tar collection can be maximized through appropriate choices of the reactor temperature, and biomass species, among others. Once the operating parameters are optimized, it is of consid-

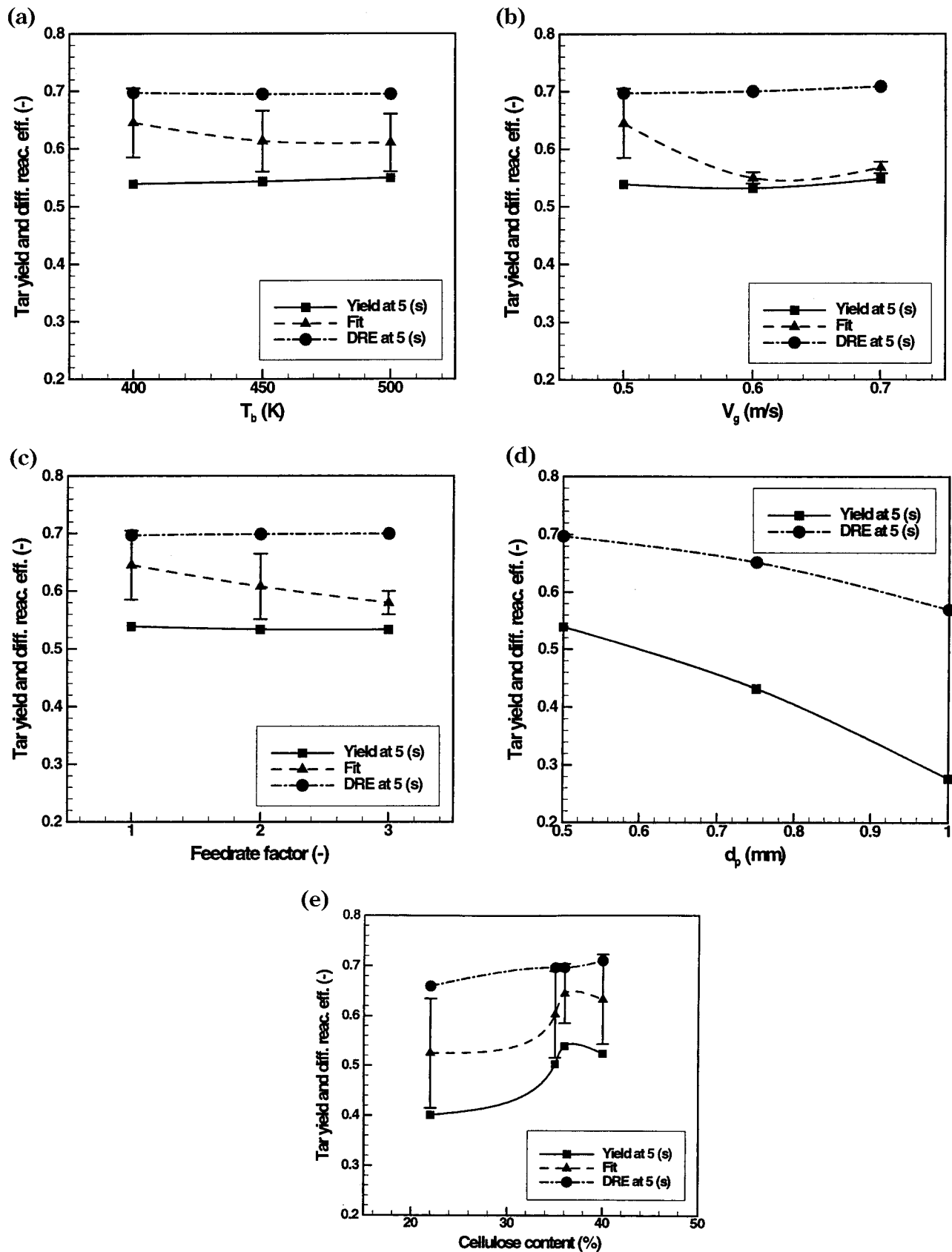


Figure 5. (a) Tar DRE, yield at 5 s, and predicted steady-state tar yield as a function of biomass injection temperatures, (b) tar DRE, yield at 5 s, and predicted steady-state tar yield as a function of fluidization fluxes, (c) tar DRE, yield at 5 s, and predicted steady-state tar yield as a function of biomass feed rate, (d) tar DRE and yield at 5 s as a function of biomass particle size, and (e) tar DRE, yield at 5 s, and predicted steady-state tar yield as a function of biomass feedstock % cellulose.

erable interest to examine whether the fluidized bed has the potential of reaching similar tar collection values

when operated at a larger scale. However, theoretical/numerical studies with respect to scale-up of fluidized

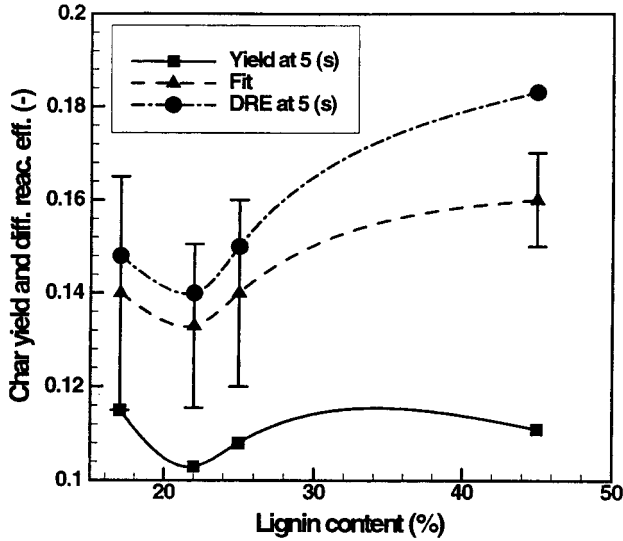


Figure 6. Char DRE, yield at 5 s, and predicted steady-state char yield as a function of biomass feedstock % lignin.

bed pyrolysis reactors are virtually absent in the literature. A notable exception is a similar investigation for maximizing tar collection in vortex pyrolysis reactors by Miller and Bellan.¹ Herein, the effects of reactor geometry and scaling are addressed in order to assess the industrial viability of the process.

Figure 7a shows the obtained tar yield at 5 s, the DRE at 5 s, and the extrapolated tar yield as function of a proportional scaling factor. Because, as discussed above, the reactor operation is a very weak function of the biomass feed rate, the pertinent quantity indicating the steady-state tar yield is the DRE. Basically, both the short-time and DRE tar collection are weak functions of the scaling factor, confirming the ideas outlined above regarding secondary tar decomposition. To further confirm this idea, a nonproportionally scaled fluidized bed has also been investigated, where the scaling in the x -direction is the same, but where the vertical size of the bed remains unchanged. Figure 7b illustrates the results of this comparison, and it can be concluded that similar results are obtained as for the proportional scaling. Only marginally better scaling is obtained in Figure 7b than in Figure 7a.

Since reactor scaling for pyrolysis applications is particularly inhibited by the associated increase in gas residence time, τ_R , and the accompanying tar-to-gas conversion mechanism, τ_{tar} , it is therefore important to minimize τ_R in order to reduce secondary production of gas. To evaluate the possibility of minimizing τ_R with respect to τ_{tar} one may estimate their ratio defined as

$$\frac{\tau_R}{\tau_{tar}} = L_y V_g A_{tar} \exp(-E_{tar}/R_u T_g) \quad (45)$$

where the kinetic parameters are those of reaction K_4 (tar-to-gas conversion), L_y is the height of the domain, and V_g is the fluidization velocity. To prevent secondary gas formation, the goal is to have $\tau_R/\tau_{tar} \ll 1$. Depicted in Figure 8 is such an estimate for several proportional scale-up factors as a function of T_g . The curves were obtained from eq 45 by fixing $V_g = 0.5$ m/s and

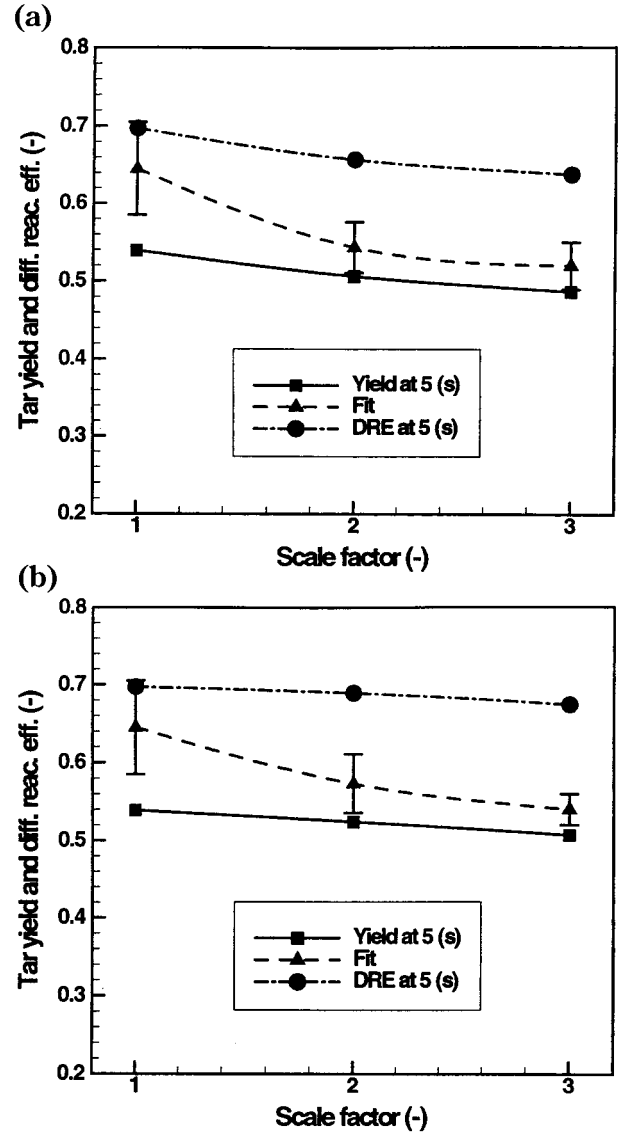


Figure 7. (a) Tar DRE, yield at 5 s, and predicted steady-state tar yield versus scale factor (1, 2, and 3) for proportional scaling. (b) tar DRE, yield at 5 s, and predicted steady-state tar yield versus scale factor (1, 2, and 3) for shallow bed scaling.

proportionally varying L_y . If one considers that $\tau_R/\tau_{tar} \sim 0.1$ represents a threshold above which tar-to-gas conversion is important, it is clear that only the standard scale reactor can operate close to the optimal temperature found from the detailed simulations; the larger scale reactors must operate at a temperature below the optimal one, or incur tar losses before collection. We note that this standard scale reactor is laboratory, rather than industrial scale.

Finally, two detailed simulations were performed with a higher V_g in a proportionally scaled bed to explicitly decrease the residence time of the gas while keeping other parameters constant. Only slight improvements in tar collection were obtained (of the order of 1%), and thus the results are not shown. This result agrees with the simple estimate provided by eq 45 where it is clear that V_g must be proportionally increased with L_y to maintain τ_R/τ_{tar} constant. Therefore, to optimize tar collection in industrial scale reactors, it is proposed that the gas fluidization velocity should be increased with the reactor height.

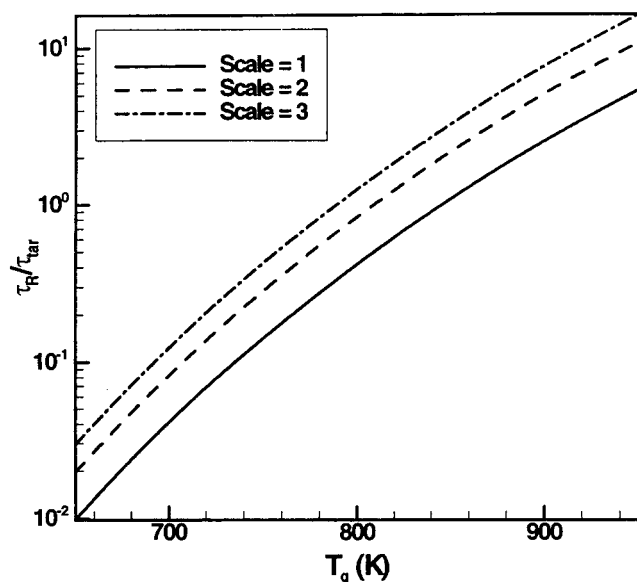


Figure 8. Ratio of the mean tar residence time to the tar-to-gas conversion kinetic time for proportional scaling.

5. Conclusions

A comprehensive mathematical model of fluidized bed reactors used for harvesting tar from biomass has been presented. The model is based on detailed submodels for the hydrodynamics of the gas–solid mixture and the biomass kinetics. The submodels were chosen for their ability to capture the relevant physics. The separately validated biomass pyrolysis kinetics model of Miller and Bellan⁴ was chosen for its ability to differentiate between the various biomass feeds available through the use of a superimposed cellulose, hemicellulose, and lignin kinetics scheme. The hydrodynamics model is based on the detailed multiphase model of Lathouwers and Bellan⁶ which is able to describe the dynamics and heat transfer of dense, reactive gas–solid mixtures. The multiphase flow mathematical description is obtained from systematic averaging of the local instantaneous equations using the kinetic theory of granular flows in combination with rigid sphere interaction models explicitly accounting for collisional transfer between the particles. This model avoids as much as possible heuristic extensions from monodisperse results which are common throughout the literature. The model was previously qualitatively and quantitatively validated against experimental data of bubbling fluidized beds. The combined submodels have been used herein to investigate the efficiency of bubbling fluidized bed reactors for condensable tar production from biomass particles by means of pyrolysis. A series of simulations has been performed in order to assess the influence of process parameters on the efficiency of the reactor, and to investigate the potential for scale-up. The present study appears to be the first in the literature where such a detailed computational study is reported in the context of biomass particle pyrolysis using bubbling fluidized bed reactors.

Results indicate that the optimum temperature for a biomass feed consisting of bagasse particles is around 750 K. The obtained tar collection at this temperature is about 0.7, which is in accordance with experimental data for various bubbling bed geometries. Higher tem-

peratures give rise to increasing gas collection at the expense of tar. At fixed particle size, the fluidizing gas temperature is the most important process parameter. Results concerning the variation of other major process parameters, such as the biomass temperature on entering the reactor, feedstock, fluidization velocity magnitude, and the biomass feed rate, indicate that tar collection displays a low sensitivity with respect to these parameters. To assess the commercial viability of the bubbling fluidized bed for pyrolysis applications, scale-up of the system has also been investigated. Scaling is found to have a small adverse effect on the tar collection capabilities at the optimal operating temperature. Shallow beds scale slightly better than those having large aspect ratios (height/width length ratio). Using a simple estimate of characteristic times, it is proposed that the fluidization velocity should be proportionally increased with reactor height to maintain minimal tar-to-gas conversion at high reactor temperatures beneficial to tar production from biomass.

Acknowledgment. This research was conducted at the Jet Propulsion Laboratory (JPL) and sponsored by the U.S. Department of Energy (DOE), with Mr. Neil Rossmeissl (DOE Headquarters) and Mr. D. Hooker (DOE Golden Center) serving as contract monitors, under an agreement with the National Aeronautics and Space Administration. Computational resources were provided by the supercomputing facility at JPL.

Nomenclature

- A = Rate constant (1/s)
- Bi = Biot number
- C = Particle velocity fluctuation (m/s)
- C_d = Drag coefficient
- C_p = Heat capacity at constant pressure ($\text{J kg}^{-1} \text{K}^{-1}$)
- \mathbf{c} = Particle velocity (m/s)
- \mathcal{D}_{ii} = Self-diffusion coefficient (m^2/s)
- \mathcal{D}_{ξ} = Gas species diffusion coefficient (m^2/s)
- d_i = Particle diameter (m)
- E^a = Activation energy (J/kmol)
- e_{ik} = Restitution coefficient
- F_{bl} = Blowing correction factor
- F_{ik} = Multiplication factor (kg/m^7)
- Fr = Frictional stress model constant (Pa)
- f = Correction factor for drag coefficient
- \mathbf{f}_g = Gravitational acceleration (m/s^2)
- $f^{(1)}$ = Single-particle distribution function ($\text{s}^3 \text{m}^{-6} \text{kg}^{-1} \text{K}^{-1}$)
- h = Specific enthalpy (J/kg)
- h_{ik} = Radial distribution function
- I = Radiation intensity (W/m^2)
- I_2 = Second invariant of strain rate tensor ($1/\text{s}^2$)
- K = Reaction rate (1/s)
- L = Macroscopic length scale (m)
- M_i = Reduced particle mass
- M_{ξ} = Total mass of species ξ in reactor (kg)
- m_i = Particle mass (kg)
- Nu = Nusselt number
- n = Frictional stress model constant
- n_i = Number density ($1/\text{m}^3$)
- $P(\Pi)$ = Probability of encountering realization Π
- Pr_g = Gas-phase Prandtl number
- p = Frictional stress model constant
- p_g = Thermodynamic pressure (Pa)
- Q_r = Radiative component of particle heat transfer (W)
- \mathbf{q} = Heat flux vector ($\text{J m}^{-2} \text{s}^{-1}$)
- \mathbf{q}_i = Collisional flux in granular energy equation (kg/s^2)

$R_{i\xi}$ = Reaction rate for phase i for species ξ (1/s)

R_u = Universal gas constant (J kmol⁻¹ K⁻¹)

Re = Particle Reynolds number

S = Strain rate tensor (1/s)

T = Temperature (K)

t = Time (s)

t_s = Start time (s)

u = Velocity vector (m/s)

V_i = Particle volume, including pores (m³)

X^c , X^h , X^l = Char ratio formed through reaction of cellulose, hemicellulose and lignin, respectively

x = Spatial coordinate (m)

x , y , z = system of coordinates (m)

Y = Species mass fraction

W = Weight function for gas-particle drag

W_ξ = Molecular weight of species ξ (kg/kmol)

Greek symbols

α = Phase fraction with pores included in gas phase

$\hat{\alpha}$ = Phase fraction with pores included in particle phase

Γ = Mass transfer rate (kg m⁻³ s⁻¹)

γ_i = Collisional source in granular energy equation (kg/ms²)

Δh = Reaction enthalpy (J/kg)

ϵ_i = Particle porosity

η_i = Particle solidity

η = Yield parameter

ϑ = Differential reactor efficiency

Θ_i = Granular temperature (m²/s²)

κ = Absorption or scattering coefficient (1/m)

λ = Thermal conductivity (W/mK)

μ = Viscosity (kg/ms)

ρ = Density (kg/m³)

Σ = Stress tensor (kg/ms²)

σ_i = Particle radius (m)

σ_B = Stefan Boltzmann constant (W m⁻² K⁻⁴)

τ_R = Mean gas residence time (s)

$\tau_{i,12}$ = Fluid particle drag time scale (s)

τ_{tar} = Secondary tar conversion time scale (s)

ϕ = Angle of internal friction (deg)

ϕ_i = Collisional source in momentum equation (kg m² s⁻²)

χ = Phase indicator

Ψ = General variable (consistent units)

Ω_ξ = Total mass of species ξ convected out the reactor (kg)

Subscripts

a = Absorption

b = Blackbody

bl = Blowing

g = Gas phase

i = Phase index

max = Maximum value

min = Minimum value

v = Vapor

x , y , z = system of coordinates (m)

ξ = Species index

Superscripts

f = Frictional

EF010053H